


Measuring densities of cold atomic clouds smaller than the resolution limitA. Litvinov,¹ P. Bataille,¹ E. Maréchal,^{1,2} P. Pedri,¹ O. Gorceix,¹ M. Robert-de-Saint-Vincent ,¹ and B. Laburthe-Tolra¹¹Laboratoire de Physique des Lasers, Université Sorbonne Paris Nord F-93430 Villetaneuse, France,
and LPL CNRS, UMR 7538, F-93430 Villetaneuse, France²Laboratoire de Physique et Etude des Matériaux (CNRS-Sorbonne Université-ESPCI), PSL Research University, F-75005 Paris, France

(Received 21 May 2021; accepted 19 July 2021; published 8 September 2021)

We propose and demonstrate an experimental method to measure by absorption imaging the size and local column density of a cloud of atoms, even when its smallest dimension is smaller than the resolution of the imaging system. To do this, we take advantage of the fact that, for a given total number of atoms, a smaller and denser cloud scatters less photons when the gas is optically thick. The method relies on making an ansatz on the cloud shape along the unresolved dimension(s) and on providing an additional information, such as the total number of atoms. We demonstrate the method on *in situ* absorption images of elongated ⁸⁷Sr Fermi gases. We find significant nonlinear corrections to the estimated size and local density of the cloud compared to a standard analysis. This allows us to recover an undistorted longitudinal density profile and to measure transverse sizes as small as one-fourth of our imaging resolution. The ultimate limit of our method is the wavelength that is used for imaging.

DOI: [10.1103/PhysRevA.104.033309](https://doi.org/10.1103/PhysRevA.104.033309)**I. INTRODUCTION**

The cold atoms community typically uses absorption imaging to explore the physics of dense clouds of atoms. In many cases, especially in the case of *in situ* observations to investigate, e.g., the equation of state of quantum fluids [1–4] or one-dimensional (1D) gases [5], these objects are extremely small and sometimes even below the resolution limit of the imaging system. More generally, quantum gases reveal interesting phenomena in small local features: vortices [6] whose size is set by condensates' healing length and typically cannot be resolved *in situ*, density fluctuations [7], Wannier functions in optical lattices, etc. Resolving such structures is a difficult but rewarding problem that prompted important technical developments, using, for example, high-resolution objectives in the quantum gas microscope approach [8] (which are nevertheless still limited to the diffraction limit), the newly demonstrated quantum gas magnifier [9], super-resolution imaging [10,11], scanning probes using electrons [12] or ions [13].

Here we focus on the *in situ* imaging of small and dense objects using standard absorption imaging. In practice, trapped gases can be both extremely absorbing and smaller than the imaging resolution, which constitutes a severe difficulty for image analysis due to, e.g., total light absorption [14] or diffraction of the optical fields used for imaging. We, nevertheless, show that it is still possible to accurately measure the size and local density of an object, even when this object is smaller than the imaging resolution.

The decrease in light intensity induced by propagation through an atomic sample can be linked to the column density thanks to the Beer-Lambert law. However, for objects smaller than the imaging resolution and when light absorption is

strong, the information on the column density is partially lost. Indeed, the Beer-Lambert law is nonlinear and cannot be averaged over the imaging resolution. Crucially, the average number of absorbed photons per atom depends on the cloud size since atoms in a smaller and therefore optically thicker medium are exposed to a reduced average light intensity. Our main idea is to take advantage of this to reconstruct information on size and local density at scales below the imaging resolution.

In the first section of this paper, we explain our image processing, which estimates the size of atomic clouds by using the nonlinearity of the Beer-Lambert law and an additional information. This latter, we here take to be an independent measurement of the total number of atoms. In the second section, we use this method to analyze images of ultracold strontium clouds at temperature ranging from $0.14T_F$ to $1.6T_F$ (where T_F is the Fermi temperature). We focus on cases where the ultracold gases have expanded while being strongly confined in two dimensions, which results in a very elongated cloud with a very small transverse dimension due to confinement and a longitudinal profile that reproduces the initial momentum distribution. This very elongated cloud and, in particular, the measurement of its transverse size is our subject of study. In practice, using the averaged Beer-Lambert law results in a loss of information on this transverse size (which is smaller than the resolution limit of our imaging system) and a strongly distorted shape along the longitudinal axis. We show that our method enables us to deduce the transverse size, which, in practice, was down to 0.25 times the imaging resolution at the lowest temperature. This transverse size is in good agreement with theoretical predictions; the longitudinal density profile deduced from our method is also in agreement with the expected Fermi distribution.

II. BEER-LAMBERT LAW FOR OBJECTS BELOW IMAGING RESOLUTION

We first describe our approach to analyze absorption images of atomic clouds smaller than the imaging system resolution. We will focus on a situation where the profile of the column density is smaller than the resolution limit in one direction only. The approach can be generalized to structures that are smaller than the imaging resolution in the two dimensions perpendicular to the propagation axis of the imaging laser beam.

Under standard conditions of imaging, the propagation along Oz of resonant light at intensities $I(x, y, z)$ below the saturation intensity, through an atomic cloud of density $n(x, y, z)$, follows the Beer-Lambert law:

$$\frac{dI(x, y, z)}{I(x, y, z)} = -n(x, y, z)\sigma_0 dz, \quad (1)$$

where $\sigma_0 = 3\lambda^2/2\pi$ is the resonant light absorption cross section for a single atom. λ is the photon wavelength. We will consider the situation where the longitudinal size of the object l along the direction of the imaging laser beam is smaller than the Rayleigh length associated with its transverse size σ , i.e., $l < \pi\sigma^2/\lambda$. In this regime, diffraction of the imaging beam as it propagates through the cloud can be neglected over the distance l such that the intensity variations along x, y, z are independent. Then Eq. (1) can be integrated to provide a measurement of the optical depth D_{opt} :

$$D_{\text{opt}}(x, y) = -\ln \frac{I(x, y)}{I_0(x, y)} = \sigma_0 \int_{-\infty}^{\infty} n(x, y, z) dz, \quad (2)$$

where $I_0(x, y)$ is the transmitted light intensity without atoms and $I(x, y)$ is the transmitted light intensity with atoms. $D_{\text{opt}}(x, y)/\sigma_0$, thus, provides the column density $\int_{\mathbb{R}} n(x, y, z) dz \equiv \tilde{n}(x, y)$.

Experimentally, information on light intensity is limited by the imaging resolution, set by, e.g., the detector pixel size, aberrations, or the diffraction limit. We, thus, consider the collected power over a size a at position $\{x = ia, y = ja\}$, characterized by the indices (i, j) ,

$$P(i, j) = \iint_{D_{i,j}} I(x, y) dx dy, \quad (3)$$

where $D_{i,j} = [\{ia, (i+1)a\}\{ja, (j+1)a\}]$ is the domain of integration. It is possible to extract density information from $\frac{P(i,j)}{P_0(i,j)}$ [where $P_0(i, j)$ is the collected power without atoms] and Eq. (2) when $I(x, y)$ varies slowly over the distance a , or when absorption is negligible. However, in general, and in the present situation,

$$\ln \left(\frac{P(i, j)}{P_0(i, j)} \right) \neq \frac{1}{a^2} \iint_{D_{i,j}} \ln \left(\frac{I(x, y)}{I_0(x, y)} \right) dx dy, \quad (4)$$

such that only measuring $P(i, j)$ and $P_0(i, j)$ is insufficient to provide information on either the peak or the averaged column density.

Nevertheless, for a given total atom number, the total absorbed light power strongly depends on the extension of the imaged object on the imaged plane when absorption is strong, irrespective of the imaging resolution. This is due to a shadowing effect in which the first atoms met by the imaging light reduce the light intensity for the subsequent atoms. This is

strongest for small size samples because of increased density. Although this effect is well captured by the Beer-Lambert law, Eq. (4) indicates deviations when information is derived from images that are pixelated or blurred at the scale of the sample size. Then, the number of absorbed photons still depends on the size of the cloud, and, as we will now see, it is still possible to deduce this size and the local density if one provides independent information, such as the total atom number.

In our experiment, the column density varies rapidly along the short axis Ox and slowly along Oy , see Fig. 1. We will now relate the total number of absorbed photons integrated along a pixel line parallel to Ox to the local column density. We define

$$R_{\text{ph}}(j) = \sum_i \frac{P_0(i, j) - P(i, j)}{P_0(i, j)}. \quad (5)$$

For brevity, we introduce $\delta I(x, y) = I_0(x, y) - I(x, y)$. We then relate the pixelated information to local intensities $I(x, y)$ using Eq. (3), and then use Eq. (2),

$$\begin{aligned} R_{\text{ph}}(j) &= \sum_i \frac{1}{P_0(i, j)} \iint_{D_{i,j}} dx dy \delta I(x, y) \\ &= \sum_i \iint_{D_{i,j}} dx dy \frac{I_0(x, y)}{P_0(i, j)} \\ &\quad \times \left[1 - \exp \left(-\sigma_0 \int_{\mathbb{R}} n(x, y, z) dz \right) \right]. \end{aligned} \quad (6)$$

The discrete indices (i, j) and the size a can be matched to physical pixels of the camera, or to effective pixels after binning. In any case, Eq. (6) is valid provided the incident intensity in the atomic plane, imaged to form $I_0(x, y)$ on the camera, is homogeneous at the spatial scale of the resolution limit of the imaging system.

To simplify Eq. (6), we note that $\frac{I_0(x, y)}{P_0(i, j)} = \frac{1}{a^2}$ and that $\sum_i \int_{ia}^{(i+1)a} dx [\dots] = \int_{\mathbb{R}} dx [\dots]$ as the integrand $[\dots]$ is zero far away from the cloud. Furthermore, in our case, the atomic density along Oy varies slowly over a pixel length such that we can also replace $\int_{ja}^{(j+1)a} dy f(y)$ [where f is the integrand over y in Eq. (6)] by $af(ja)$.

Our idea is to introduce an ansatz on the local column density profile along Ox , which for simplicity is taken as Gaussian,

$$\tilde{n}(x, y) = e^{-(x^2/2\sigma_x^2)} \tilde{n}(0, y), \quad (7)$$

Then, in the integration along x of Eq. (6) we apply a change in variable $u = x/\sigma_x$. We obtain

$$\begin{aligned} R_{\text{ph}}(j) &= \frac{\sigma_x}{a} \int_{\mathbb{R}} [1 - \exp(-\sigma_0 \tilde{n}(0, aj) e^{-(u^2/2)})] du \\ &\equiv \frac{\sigma_x}{a} F(\sigma_0 \tilde{n}(0, aj)), \end{aligned} \quad (8)$$

where we defined the transfer function F .

The total number of atoms N_{at} can be computed according to the definition of the column density and to Eq. (7), and related to R_{ph} using Eq. (8),

$$N_{\text{at}} = \frac{\sqrt{2\pi} a \sigma_x}{\sigma_0} \sum_j F^{-1} \left(\frac{a}{\sigma_x} R_{\text{ph}}(j) \right). \quad (9)$$

To obtain these equations, four assumptions have been made. First, the density along the short axis Ox is assumed

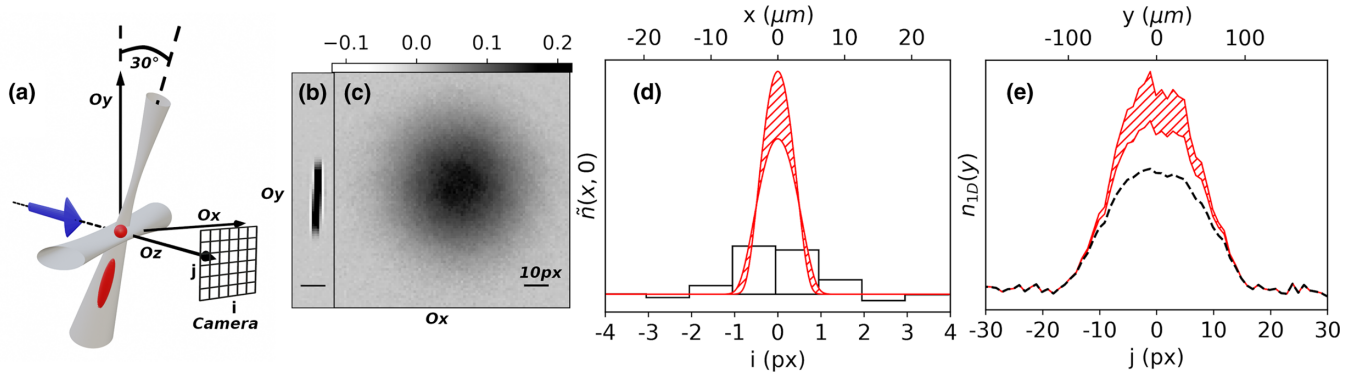


FIG. 1. Recovering density profiles from distorted absorption images of tightly confined gases. (a) Geometry. (b) Absorption image of a gas tightly confined and expanding in one dimension. (c) Time-of-flight absorption image when the gas is released in all three directions. (d) Cross section along the short axis of the column density shown in (b) at peak value. The raw data (column density deduced from the pixelated optical depth) shows diffraction fringes locally leading to nonphysical negative optical depth (black squares). Our method does not use the optical depth but rather estimates density by counting missing photons and assuming a Gaussian shape to the cloud in its shortest dimension. The result of our method is shown by the red solid lines, delimiting a confidence interval (red hashes) resulting from experimental fluctuations. The raw data underestimate the atom number by a factor of 1.5 and the peak column density by a factor of roughly 4 in this case. Our method allows to infer an object size of only 0.25 px (pixel size). (e) Linear density along the long axis Oy , $n_{1D}(y)$ deduced either by integrating the pixelated optical depth along the short axis Ox (black dashes) or by our method (red solid lines, delimiting the confidence interval).

to be a Gaussian of width σ_x . Second, the column density $\tilde{n}(x=0, y)$ along the long axis Oy is quasiuniform along the width of a pixel. Third, the illumination is homogeneous at the scale of the resolution limit. Finally, we also assumed that diffraction of the probe light by the atomic sample can be neglected over the depth of the sample along Oz so that the Beer-Lambert law can be applied locally.

Both Eqs. (8) and (9) give the possibility to reconstruct the actual density profiles even when the Beer-Lambert law cannot be directly used on the raw data. Indeed, F is nonlinear so that a given density profile $\tilde{n}(0, aj)$ results in distorted profiles $R_{ph}(j)$ that parametrically depend on σ_x . Therefore, we can, in principle, retrieve the transverse size σ_x from Eq. (8) when the longitudinal density profile is known *a priori*. This is the case, for example, in our experiment at high temperature where the longitudinal cloud shape along Oy should obey Boltzmann statistics and be Gaussian. Alternatively Eq. (9) simply relates the free unknown parameter σ_x to the total number of atoms, which is useful provided this number can be measured independently.

In what follows, we obtain N_{at} by an independent measurement on expanded clouds for which the gas is larger than the resolution in three dimensions (3D) so that the usual analysis holds and $N_{at}^{3D} = \frac{a^2}{\sigma_0^2} \sum_{i,j} D_{opt}^{3D}(i, j)$ (D_{opt}^{3D} is the optical depth for the images with 3D expansion). We point out that the estimate of σ_x that we, thus, perform is independent from uncertainties in σ_0 (uncertainties that can arise, for example, for atoms with a hyperfine structure due to optical pumping effects during the imaging pulse). Indeed, setting $N_{at} = N_{at}^{3D}$ from the explicit expressions of N_{at} and N_{at}^{3D} it follows immediately that σ_x is independent of σ_0 .

III. EXPERIMENTAL RESULTS

In our experiment, whose setup is detailed in Ref. [15], the ^{87}Sr cold atomic sample is obtained after evaporation to reach regimes from $T \simeq 2T_F$ down to $T \simeq 0.15T_F$. The

optical dipole trap is made of a horizontal anisotropic laser beam crossed by a second laser beam at 30° from vertical, see Fig. 1(a). To produce a tightly confined gas in one dimension, we switch the horizontal beam off. This allows for an expansion of the gas channeled by the second laser beam for times ranging from 0.1 to 20 ms. We then take an absorption image, see Fig. 1(b), using a pulse of circularly polarized resonant light whose intensity is about 50 times below the saturation intensity, and a nonmagnifying imaging system that uses a telescope configuration to approximately conjugate the atomic plane to a CCD chip with $6.5\text{-}\mu\text{m}$ -wide pixels. The telescope is made of two achromatic lenses of local length $f = 150$ mm and diameter 50 mm. The opening diameter is set to 30 mm to reduce geometrical aberrations, and the diffraction-limited resolution corresponds to $2.8\ \mu\text{m}$. However, in practice, the resolution of our imaging system is limited by the pixel size of the CCD chip. Furthermore, as a function of time, the cloud is positioned at different depths z along the imaging axis due to the orientation of the guiding beam [see Fig. 1(a)]. This results in images that can be slightly out of focus. To independently calibrate the number of atoms, we release the gas by switching off both trapping lasers and take absorption images after a three-dimensional free flight, see Fig. 1(c).

As can be seen in Fig. 1(b), images of tightly confined gases are affected by pixelation and diffraction fringes perpendicular to the elongated direction. Figure 1(d) shows a cut through those fringes, which are visible because the object is slightly out of focus. The only diffraction signature is along the transverse axis and arises because of fast variations of the atomic density along this axis. Thus, the light is redistributed along this direction only. Therefore, we can measure $R_{ph}(j)$ on camera pixel lines without binning, even when the pixel size a is smaller than the actual optical resolution on out-of-focus clouds. Using Eq. (8) we deduce the transverse size and the local density profile of the gas, also shown in Fig. 1(d).

Our approach, thus, recovers the local peak density from which we also infer the actual density profile along the

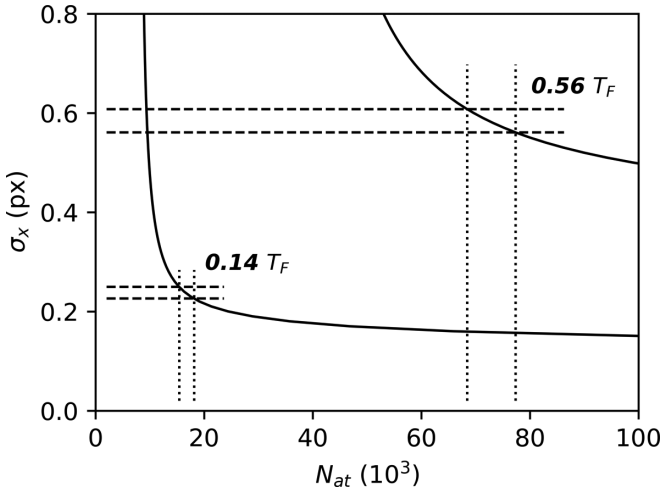


FIG. 2. Determination of σ_x based on the independently measured total atom number N_{at} , for two images (at $0.14T_F$ and $0.56T_F$) whose peak optical depths significantly differ. The black line is the inverse of Eq. (9) for a specific R_{ph} , i.e., a single image. The atom number confidence intervals (delimited by the dotted lines) are due to atom number fluctuations from shot to shot and are the dominant cause for the σ_x confidence intervals (delimited by the dashed lines). Qualitatively, a low optical depth results in a large slope and, thus, large σ_x uncertainty.

elongated axis. As shown in Fig. 1(e) the linear density derived by integrating the pixelated optical depth has a distorted shape compared to the linear density as recovered by our method. As far as the low-density part is concerned, the reconstructed profile matches that deduced from integrating the pixelated optical depth as expected for low absorption. In contrast, the high-density region, corresponding to larger absorption, is underestimated when using the pixelated optical depth.

A. Analysis of the subresolution transverse size

We now focus on our measurements of σ_x . Figure 2 illustrates how the atom number from reference images is used to recover σ_x . For a given picture of the elongated cloud, we compute $R_{\text{ph}}(j)$, we plot the number of atoms N_{at} deduced from Eq. (9) as a function of an assumed value of σ_x . From the reference measurement of $N_{\text{at}}^{3\text{D}}$ and its uncertainty associated with shot-to-shot fluctuations, we deduce the corresponding value and confidence interval of σ_x that we will present in the following figures.

In Fig. 3 we observe that σ_x does not vary much with the guided time of flight (its variations are similar to the approximately 10% standard deviations of the data). Such a small variation is expected because the gas evolves while being confined in the guiding beam with a transverse confinement frequency which we estimate to vary from 210 Hz at the initial position to 145 Hz after 20 ms of guided fall. Indeed, if we assume that the transverse degrees of freedom follow adiabatically such an evolution, the decrease in trapping frequency corresponds to an increase of only 20% in the transverse size. Our ability to measure σ_x for a large range of expansion times illustrates the robustness of the method as from the short to

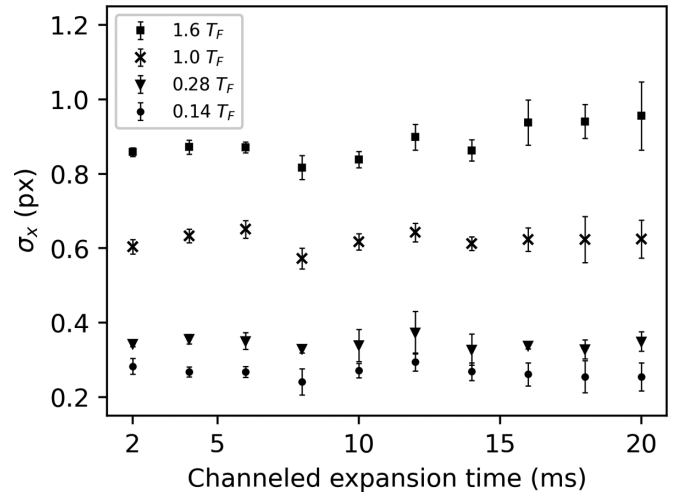


FIG. 3. Time dependence of σ_x from 2 to 20 ms channeled expansion at different degeneracies. Each point aggregates typically ten images with error bars that show the standard deviations between the individual measurements. Those standard deviations match the individual picture confidence interval (see Fig. 2) and, thus, can be attributed to mostly measurement uncertainty. The degeneracy is deduced from the reference images.

long time of flight the peak optical density varies by a factor of 14 because of the longitudinal expansion. Furthermore, the method provides accurate estimates of σ_x even for short expansion times (2 ms), which indicates that the longitudinal profile varies slowly enough for the approximation made to derive Eq. (8) to remain valid.

As shown in Fig. 4, σ_x depends on the temperature and reaches 0.25 times the pixel size at lowest temperatures $T \simeq 30$ nK at $0.14T_F$. This value of, i.e., $1.6 \mu\text{m}$, is smaller than the typical distortions introduced by diffraction of the imaging beam and out-of-focus measurements. It is also smaller than

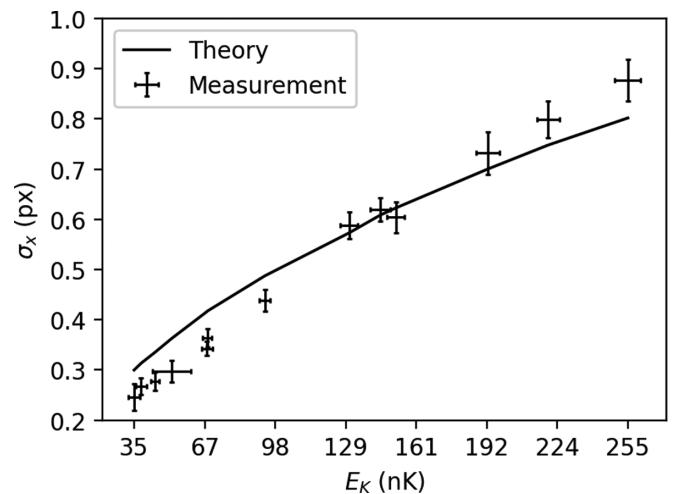


FIG. 4. Dependence of σ_x as a function of kinetic energy along one direction. The kinetic energy is deduced from the reference images. The black line shows the expected size according to equipartition of energy. The error bars show the standard deviations, aggregating data for all channeled expansion times.

the ultimate resolution of our imaging system (set by the pixel size).

To compare our measurements to theoretical expectations, we use the reference images of 3D expansions, and we measure the mean kinetic energy along the longitudinal axis E_K . Based on the equipartition of energy, and neglecting interatomic interactions, we expect $\frac{1}{2}m\omega^2\sigma_{\text{th}}^2 = E_K$. In Fig. 4, we, thus, compare the measured dependence of σ_x as a function of the energy per atom to the expected values of σ_{th} , using the independently measured initial trap confinement frequency. We find an overall good agreement with this rough theoretical model without a free parameter with discrepancies smaller than 15% throughout the curve. We point out that, based on the resolution of the Boltzmann equations [16], we expect interaction effects on the measurement of E_K during the expansion to be on the order of 8% at the lowest temperature given our experimental parameters [17], whereas the interaction effects on σ_x are on the order of 1%.

B. Longitudinal profile

In order to further verify that our results match the ones that are expected from the theoretical point of view, we now turn to the longitudinal profiles that we obtain and compare them to theory. In Fig. 5, we present both the longitudinal density profile deduced from the pixelated optical depth and the 1D density profile n_{1D} deduced from our method.

Figure 5(a) shows a nondegenerate gas at $1.6T_F$ after a channeled expansion of 10 ms. For such a long expansion, the longitudinal profile should reflect the momentum distribution along this axis before expansion. Both profiles are fitted by Gaussian distributions since at this temperature the momentum distribution is almost perfectly described by Boltzmann statistics. The residuals to the fits show that the 1D profile deduced from the pixelated optical depth (upper residuals) systematically distorts the shape of the cloud, whereas our reconstruction method (lower residuals) naturally recovers the expected Gaussian profile.

As shown in Fig. 1(a), this expansion is performed along an axis that makes an angle with the imaging plane, which defines a parallax for our measurements. In addition, during the expansion, the atoms feel a position-dependent potential due to the divergence of the Gaussian laser beam. In practice, this results in an anticonfinement. The parallax and anticonfinement can both be measured by comparing the size of the expanding cloud to its temperature and measuring the trajectory of the center of mass. For the analysis shown in Fig. 5, the parallax and anticonfinement simply result in a single multiplicative correction parameter C to the cloud size for a given expansion time.

Figure 5(b) shows the linear density of a degenerate gas at $0.21T_F$. We compare it to the expected density profile of a degenerate Fermi gas expanding in 1D. There are no free parameters since this density profile only depends on the number of atoms, the temperature, and degeneracy, which are all measured from the reference images, and C , measured from Fig. 5(a). Obviously, the linear density profile from pixelated data is in severe disagreement with the theoretical model, unlike the reconstructed profile. The agreement with this latter profile is good throughout the curve as can be seen

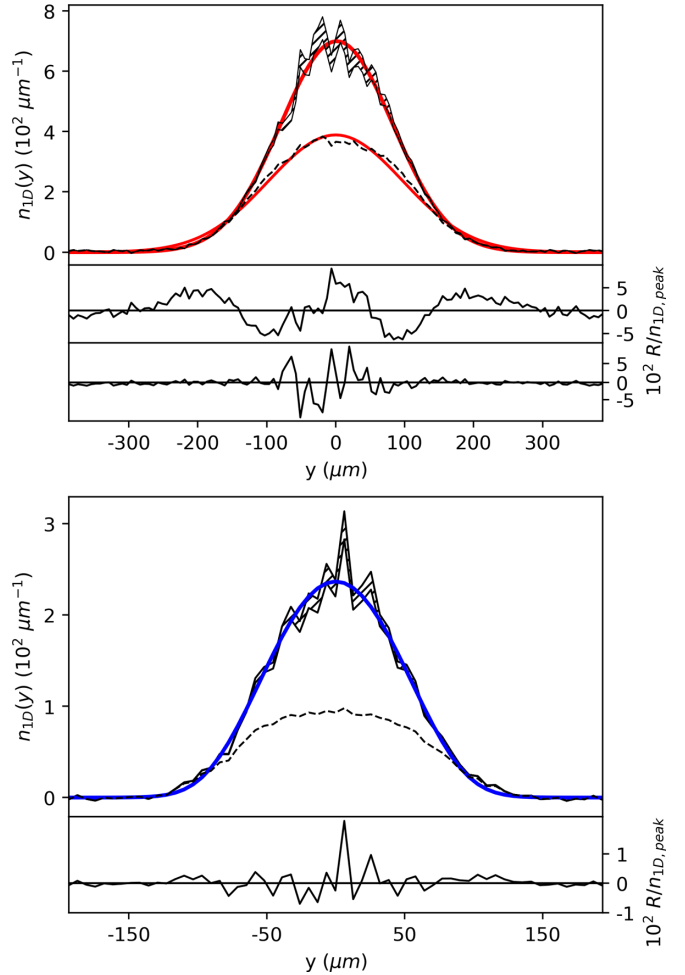


FIG. 5. Density profiles along the long axis Oy . The black hashed surface is the confidence interval on the measured $n_{1D}(y)$. The dashed line corresponds to the density deduced from the pixelated optical depth. (a) Nondegenerate gas at $1.6T_F$ after a 10-ms guided expansion. The red lines are Gaussian fits for the linear density deduced from the pixelated optical depth (upper normalized residual) and for $n_{1D}(y)$ (lower normalized residual). The residuals show that the raw data differ significantly from the expected Gaussian shape of a thermal gas. On the contrary, our method recovers this expected Gaussian shape. (b) Degenerate gas at $0.21T_F$ after an 18-ms guided expansion. In blue, the expected density profile (with no free parameter) matches the profile recovered by our method as demonstrated by the residuals shown below.

from the residuals. However, for the lowest momenta, we also observe a strong noise that affects the reconstruction. These irregularities are due to the strong nonlinearity of the transfer function F at high density. This nonlinearity may also bias an initially symmetric noise. This constitutes a limitation to our reconstruction scheme when the source of the noise is purely from technical origin; however, it also signals that our method could unveil density fluctuations that would otherwise be washed out by the limited optical resolution.

IV. DISCUSSION AND CONCLUSION

We introduced a method to analyze absorption images and to measure density profiles at scales below the imaging

resolution limit that may occur due to, e.g., pixelation, distortion of the images caused by aberrations, and the diffraction by the numerical aperture. These limitations are well known in the community and make the analysis of very small objects particularly difficult. Here we go beyond the approach performed in Refs. [18,19] that corrects the absorption by a simple numerical factor. Since the deviation to the Beer-Lambert law is nonlinear, we find that it is important to follow such a procedure as presented here in order to recover the exact local density and an undistorted density profile, even along the direction in which the cloud is larger than the imaging resolution.

In our experiment, we characterize objects as small as 0.25 times our pixel size, despite diffraction fringes due to out of focus imaging as large as two pixels—these objects are, thus, significantly below our resolution limit. Comparisons with theoretical models of the cloud shape with no free parameter confirm the validity of these results. We have further checked our method by testing its sensitivity to the ansatz that is chosen for the transverse profile. We found that using a Fermi distribution in the transverse profile barely modifies our results. This good agreement relies on a certain similarity between the actual density profile and the chosen ansatz. However, our method would not be able to reveal *unexpected* features in the shape along the nonresolved direction since different density shapes could lead to the same number of scattered photons.

We point out that although our method allows retrieving features below the imaging resolution, its fundamental limit is $\simeq \lambda$ as λ sets the scattering cross section of light by the atoms. As a consequence, an object whose size would be below λ would affect light propagation identically irrespective of its actual size. In addition to this limit on the transverse size σ , there is also a limitation associated with the depth l of the object along the axis of the imaging beam. For our equations to hold, it is necessary that the diffraction of the light field can be neglected over the distance l . Therefore, it is important that $l < \pi \sigma^2 / \lambda$.

Finally, we point out that our method could easily be generalized to study features smaller than the imaging resolution within clouds otherwise larger than the imaging resolution. For example, using the appropriate ansatz, we have in mind to measure the size of vortex cores within a two-dimensional or a 3D superfluid, that are typically below the imaging resolution, or other hydrodynamic structures, such as solitons [20].

ACKNOWLEDGMENTS

This research was funded by the Agence Nationale de la Recherche (Projects No. ANR-18-CE47-0004 and No. ANR-16-TERC-0015-01), the Conseil Regional d'Ile-de-France, Institut Francilien des Atomes Froids, DIM Nano'K (Projects METROSPIN and ACOST), DIM Sirteq (Project SureSpin), and Labex FIRST-TF (Project CUSAS).

-
- [1] Y. Shin *et al.*, *Nature (London)* **451**, 689 (2008); *Phys. Rev. A* **77**, 041603(R) (2008).
 - [2] T. Ho and Q. Zhou, *Nat. Phys.* **6**, 131 (2009).
 - [3] S. Nascimbene *et al.*, *Nature (London)* **463**, 1057 (2010).
 - [4] T. Yefsah, R. Desbuquois, L. Chomaz, K. J. Günter, and J. Dalibard, *Phys. Rev. Lett.* **107**, 130401 (2011).
 - [5] M. A. Cazalilla, R. Citro, T. Giamarchi, E. Orignac, and M. Rigol, *Rev. Mod. Phys.* **83**, 1405 (2011).
 - [6] M. R. Matthews, B. P. Anderson, P. C. Haljan, D. S. Hall, C. E. Wieman, and E. A. Cornell, *Phys. Rev. Lett.* **83**, 2498 (1999); B. P. Anderson, P. C. Haljan, C. E. Wieman, and E. A. Cornell, *ibid.* **85**, 2857 (2000); K. W. Madison, F. Chevy, W. Wohlleben, and J. Dalibard, *ibid.* **84**, 806 (2000); J. R. Abo-Shaeer *et al.*, *Science* **292**, 476 (2001); E. Hodby, G. Hechenblaikner, S. A. Hopkins, O. M. Marago, and C. J. Foot, *Phys. Rev. Lett.* **88**, 010405 (2001); C. Raman, J. R. Abo-Shaeer, J. M. Vogels, K. Xu, and W. Ketterle, *ibid.* **87**, 210402 (2001); Zwierlein *et al.*, *Nature (London)* **435**, 1047 (2005).
 - [7] R. N. Bisset, C. Ticknor, and P. B. Blakie, *Phys. Rev. A* **88**, 063624 (2013).
 - [8] C. Gross and I. Bloch, *Science* **357**, 995 (2017).
 - [9] L. Asteria, H. P. Zahn, M. N. Kosch, K. Sengstock, and C. Weitenberg, [arXiv:2104.10089](https://arxiv.org/abs/2104.10089).
 - [10] S. Subhankar, Y. Wang, T.-C. Tsui, S. L. Rolston, and J. V. Porto, *Phys. Rev. X* **9**, 021002 (2019).
 - [11] M. McDonald, J. Trisnadi, K.-X. Yao, and C. Chin, *Phys. Rev. X* **9**, 021001 (2019).
 - [12] P. Würtz, T. Langen, T. Gericke, A. Koglbauer, and H. Ott, *Phys. Rev. Lett.* **103**, 080404 (2009).
 - [13] C. Veit, N. Zuber, O.-A. Herrera-Sancho, V. S. V. Anasuri, T. Schmid, F. Meinert, R. Löw, and T. Pfau, *Phys. Rev. X* **11**, 011036 (2021).
 - [14] G. Reinaudi *et al.*, *Opt. Lett.* **32**, 3143 (2007).
 - [15] P. Bataille, A. Litvinov, I. Manai, J. Huckans, F. Wiotte, A. Kaladjian, O. Gorceix, M. Maréchal, B. Laburthe-Tolra, and M. Robert-de-Saint-Vincent, *Phys. Rev. A* **102**, 013317 (2020).
 - [16] C. Menotti, P. Pedri, and S. Stringari, *Phys. Rev. Lett.* **89**, 250402 (2002).
 - [17] L. Sonderhouse *et al.*, *Nat. Phys.* **16**, 1216 (2020).
 - [18] J. Esteve, J.-B. Trebbia, T. Schumm, A. Aspect, C. I. Westbrook, and I. Bouchoule, *Phys. Rev. Lett.* **96**, 130403 (2006).
 - [19] J. Armijo, T. Jacqmin, K. V. Kheruntsyan, and I. Bouchoule, *Phys. Rev. Lett.* **105**, 230402 (2010).
 - [20] J. Denschlag *et al.*, *Science* **287**, 97 (2000).